orientational dynamics are expected to occur on a time scale significantly longer than the bulk molecular reorientational time of 1.5 ps (*21*). For water molecules surrounded by acetone (*22*) and in reverse micelles (*24*, *25*), the reorientational time was found to be at least 6 ps (*26*).

Our results appear to reflect the fundamental dynamics of the OH stretch modes and associated H bonds connecting neighbors and, as such, are insensitive to the detailed configuration of the H-bonding network. They support the general proposition that vibrational excitation and relaxation of H-bonding molecules in condensed media are governed by vibrational relaxation and energy transfer through H bonds. The experimental technique successfully demonstrated here should also open broad opportunities for ultrafast surface dynamic studies of liquids in general.

References and Notes

1. G. E. Brown Jr. *et al.*, *Chem. Rev.* **99**, 77 (1999).
2. B. C. Garrett, *Science* **303**, 1146 (2004).
3. F. Franks, *Water, a Comprehensive Treatise* (Plenum, New York, 1972).
4. M. L. Cowan *et al.*, *Nature* **434**, 199 (2005).
5. C. P. Lawrence, J. L. Skinner, *J. Chem. Phys.* **118**, 264 (2003).
6. K. B. Moller, R. Rey, J. T. Hynes, *J. Phys. Chem. A* **108**, 1275 (2004).
7. S. Woutersen, U. Emmerichs, H.-K. Nienhuys, H. J. Bakker, *Phys. Rev. Lett.* **81**, 1106 (1998).
8. Q. Du, E. Freysz, Y. R. Shen, *Science* **264**, 826 (1994).
9. Q. Du, E. Freysz, Y. R. Shen, *Phys. Rev. Lett.* **72**, 238 (1994).
10. Q. Du, R. Superfine, E. Freysz, Y. R. Shen, *Phys. Rev. Lett.* **70**, 2313 (1993).
11. J. C. Conboy, J. L. Daschbach, G. L. Richmond, *J. Phys. Chem.* **98**, 9688 (1994).
12. V. Ostroverkhov, G. A. Waychunas, Y. R. Shen, *Chem. Phys. Lett.* **386**, 144 (2004).
13. A. J. Lock, H. J. Bakker, *J. Chem. Phys.* **117**, 1708 (2002).
14. A. J. Lock, S. Woutersen, H. J. Bakker, *J. Phys. Chem. A* **105**, 1238 (2001).
15. Y. R. Shen, in *Frontiers in Laser Spectroscopy*, T. W. Hansch, M. Inguscio, Eds. (North Holland, Amsterdam, 1994), p. 139.
16. S. Woutersen, H. J. Bakker, *Nature* **402**, 507 (1999).
17. J. A. Poulsen, G. Nyman, S. Nordholm, *J. Phys. Chem. A* **107**, 8420 (2003).
18. N. Huse, S. Ashihara, E. T. J. Nibbering, T. Elsaesser, *Chem. Phys. Lett.* **404**, 389 (2005).
19. P. Guyot-Sionnest, *Phys. Rev. Lett.* **66**, 1489 (1991).
20. J. Stenger, D. Madsen, P. Hamm, E. T. J. Nibbering, T. Elsaesser, *J. Phys. Chem. A* **106**, 2341 (2002).
21. T. Steinel, J. B. Asbury, J. R. Zheng, M. D. Fayer, *J. Phys. Chem. A* **108**, 10957 (2004).
22. J. J. Gilijamse, A. J. Lock, H. J. Bakker, *Proc. Natl. Acad. Sci. U.S.A.* **102**, 3202 (2005).
23. The thermalized SF spectrum after long pump-probe delay appears blue-shifted with respect to the unpumped SF spectrum, but the blue shift is somewhat different from that observed in the IR transient absorption spectrum of bulk water (*13*, *14*). This is because the SF spectrum of the water-silica interface has a different temperature dependence (*9*) than that of the IR absorption of bulk water.
24. H.-S. Tan, I. R. Piletic, M. D. Fayer, *J. Chem. Phys.* **122**, 174501 (2005).
25. M. R. Harpham, B. M. Ladanyi, N. E. Levinger, K. W. Herwig, *J. Chem. Phys.* **121**, 7855 (2004).
26. Resonant energy transfer among OH stretch modes may also result in temporal variation of the orientational distribution of interfacial molecular excitations. Such orientational dynamics are not important for the bonded OH stretch region in our study because it is more or less complete in 100 fs. For the dangling OH stretch, resonant energy transfer between dangling OH bonds is expected to occur on a time scale much longer than 1 ps, outside the range of interest. This is because the transfer rate depends on the bond-bond distance (r) as $1/r^6$ (*16*), and r for dangling OH is larger than the nearest-neighbor distance between bonded OH, considering that there is only a quarter monolayer of them at the interface (*8*).

27. This work was supported by the Director, Office of Science, Office of Basic Energy Sciences, Materials Sciences and Engineering Division, of the U.S. Department of Energy under contract no. DE-AC03-76SF00098.

20 June 2006; accepted 17 August 2006
10.1126/science.1131536

Phase Separation of Lipid Membranes Analyzed with High-Resolution Secondary Ion Mass Spectrometry

Mary L. Kraft,[1] Peter K. Weber,[2] Marjorie L. Longo,[3] Ian D. Hutcheon,[2] Steven G. Boxer[1]*

Lateral variations in membrane composition are postulated to play a central role in many cellular events, but it has been difficult to probe membrane composition and organization on length scales of tens to hundreds of nanometers. We present a high-resolution imaging secondary ion mass spectrometry technique to reveal the lipid distribution within a phase-separated membrane with a lateral resolution of ~100 nanometers. Quantitative information about the chemical composition within small lipid domains was obtained with the use of isotopic labels to identify each molecular species. Composition variations were detected within some domains.

Imaging and quantifying the static and dynamic variations in lateral composition that result from interactions among membrane components is a major challenge in structural biology. Although biological membranes are fluid structures and fluidity is essential for function, it is widely believed that some degree of lateral organization is present and that this organization is also essential for function (*1*–*3*). The relevant distance scale is larger than that of individual membrane proteins or protein assemblies (>10 nm), whose structures can be determined by x-ray crystallography or inferred from atomic force microscopy (AFM), but is substantially below the diffraction limit of light microscopy. Fluorescence microscopy is widely used and is extremely sensitive and specific to the labeled component (*4*–*8*), but only the labeled component is observed, and, at least for relatively small components such as lipids, the fluorophore may greatly alter the delicate interactions that are present in the membrane (*9*). Infrared (*10*) and coherent anti–Stokes Raman (*11*) imaging offer greater chemical specificity, but thus far the lateral resolution and sensitivity are limited. AFM provides much better resolution of topographical features but does not yield information on chemical composition (*9*, *12*–*14*). Imaging mass spectrometry offers distinct advantages over these methods (*15*–*21*), and we applied this approach to imaging and analyzing the chemical composition of small lipid domains with lateral resolution of ~100 nm.

Secondary ion mass spectrometry (SIMS) was performed with a NanoSIMS 50 (Cameca Instruments, Courbevoie, France). During NanoSIMS analysis, a focused $^{133}Cs^+$ primary ion beam is rastered across the sample; secondary ions generated by sputtering are extracted and analyzed according to their respective charge-to-mass ratios at high mass resolving power (Fig. 1). By selectively incorporating a distinctive stable isotope into each membrane component [e.g., ^{13}C or ^{15}N], NanoSIMS secondary ion images characteristic of each species [e.g., $^{13}C^1H^-$ or $^{12}C^{15}N^-$, respectively] can be used to create a component-specific compositional map of the sample. We used this approach to demonstrate the ability to image and analyze quantitatively the composition of very small lipid domains within a phase-separated lipid membrane.

Supported lipid bilayers were prepared from vesicles containing equal mole fractions of ^{15}N-labeled 1,2-dilauroylphosphatidylcholine [^{15}N-DLPC, melting temperature (T_m) = –1°C] and ^{13}C-labeled 1,2-distearoylphosphatidylcholine ($^{13}C_{18}$-DSPC, T_m = 55°C), with 0.5 mol % of a fluorescent lipid added to allow the bilayer quality to be evaluated by fluorescence microscopy during sample preparation (*22*). The sample was maintained at 70°C (above the T_m of both lipid components) to ensure complete mixing, both during vesicle and supported bilayer formation on prewarmed (70°C) silicon wafers. The silicon wafers were prepared with a thin (17 nm) SiO_2 layer that facilitated the formation of stable bilayers while permitting charge dissipation during the SIMS analysis,

[1]Department of Chemistry, Stanford University, Stanford, CA 94305, USA. [2]Glenn T. Seaborg Institute & BioSecurity and Nanosciences Laboratory, Lawrence Livermore National Laboratory, Livermore, CA 94551, USA. [3]Department of Chemical Engineering and Materials Science, University of California, Davis, CA 95616, USA.

*To whom correspondence should be addressed. E-mail: sboxer@stanford.edu

and the wafers were patterned with chrome grids to corral the lipid bilayers and provide landmarks on the surface for characterization of the same regions by fluorescence, AFM, and NanoSIMS imaging (*22*, *23*). The homogeneous, supported bilayer samples were slowly cooled to room temperature to induce phase separation (Fig. 1), rapidly frozen, and freeze-dried to remove water without disrupting the lateral organization within the membrane (fig. S1). Note that the lipid bilayers are fully hydrated before being frozen. Before NanoSIMS analysis, the geometries of the gel-phase domains, which are thicker than the fluid-phase regions, were characterized by AFM for subsequent comparison to the NanoSIMS data. As shown in Fig. 2D, the AFM image of the freeze-dried supported lipid bilayer contained domains that extended ~2.0 nm above the neighboring bilayer, in good agreement with the reported height difference (1.8 nm) between gel-phase DSPC and fluid-phase DLPC in a hydrated supported lipid bilayer on mica (*24*, *25*).

For chemical imaging, the $^{13}C^{1}H^{-}$ and $^{12}C^{15}N^{-}$ NanoSIMS secondary ion signals were used to evaluate the distributions of $^{13}C_{18}$-DSPC and ^{15}N-DLPC, respectively, within the supported lipid bilayer. Although other secondary ions with nominal masses of 14 amu ($^{12}C^{1}H_{2}^{-}$) and 27 amu ($^{13}C^{14}N^{-}$) were generated during analysis, the mass resolving power was sufficient to resolve the $^{13}C^{1}H^{-}$ and $^{12}C^{15}N^{-}$ ions from these interfering isobars while maintaining high lateral resolution, which permitted unambiguous identification of the species of interest. The component-specific NanoSIMS secondary ion images in Fig. 2, A to C, show that the bilayer was not homogeneous. Distinct microdomains enriched in $^{13}C_{18}$-DSPC, as evidenced by an increased $^{13}C^{1}H^{-}$ signal and decreased $^{12}C^{15}N^{-}$ signal, were dispersed within a ^{15}N-DLPC–rich matrix. The area occupied by $^{13}C_{18}$-DSPC within the bilayer was lower than that based on the molar ratio of the lipids in the vesicle solution as prepared. This difference in the lipid composition between the vesicle solution and the phase-separated supported lipid bilayer is likely due to selective adsorption of these very different lipid species (*26*).

Close examination of the sizes and shapes of the $^{13}C_{18}$-DSPC–enriched domains observed in the NanoSIMS secondary ion images revealed that they were nearly identical to the domain geometry imaged by AFM at the same sample locations (Fig. 2D). Phase-separated domains with complex edge structures and domains as small as ~100 nm in diameter, as measured by AFM, are visible in the NanoSIMS secondary ion images (Fig. 2, circles), confirming the high lateral resolution and sensitivity of the NanoSIMS technique. A few of the features in the AFM image did not produce lipid-specific secondary ion signals (Fig. 2, arrows); the height difference between these features and the bilayer (>5 nm, measured by AFM) confirmed that these objects were unlabeled debris and not lipid domains.

Quantitative information on the lipid composition within specified regions of the bilayer was obtained by calibrating the secondary ion yields against standard samples (*22*). Briefly, NanoSIMS measurements were made on sets of homogeneous supported lipid bilayers that systematically varied in the $^{13}C_{18}$-DSPC or ^{15}N-DLPC content, and calibration curves were constructed that correlated the normal-

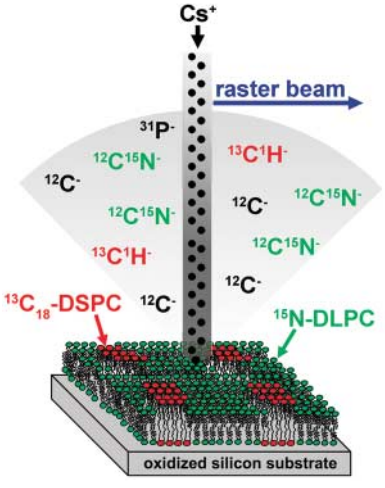

Fig. 1. Schematic showing NanoSIMS analysis of phase-separated lipid bilayer (not to scale). At room temperature, gel and fluid phases, mostly composed of $^{13}C_{18}$-DSPC (red) and ^{15}N-DLPC (green), respectively, are present in the bilayer. The gel phase is ~2 nm higher than the neighboring fluid phase and can be imaged by AFM (compare with Fig. 2D). The sample is freeze-dried to preserve the lateral organization within the bilayer (fig. S1) and analyzed with the NanoSIMS. During NanoSIMS analysis, a focused $^{133}Cs^{+}$ ion beam generates secondary ions; the negative ions are collected and analyzed in a high-resolution mass spectrometer. The secondary ions that are characteristic of $^{13}C_{18}$-DSPC and ^{15}N-DLPC ($^{13}C^{1}H^{-}$ and $^{12}C^{15}N^{-}$, respectively) are used to identify each component in the NanoSIMS image. The $^{133}Cs^{+}$ primary ion beam is focused to a spot ~100 nm in diameter (fig. S2) and is rastered across the sample to generate an image.

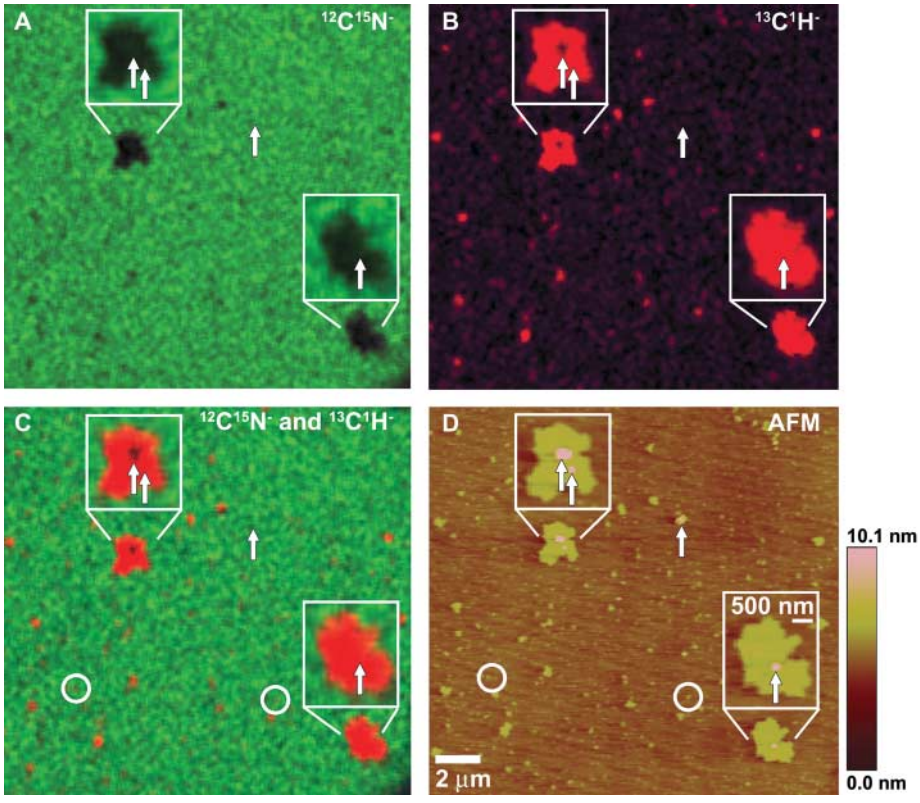

Fig. 2. A phase-separated supported lipid bilayer that was freeze-dried and imaged by NanoSIMS and AFM. (**A** to **C**) NanoSIMS images of the normalized $^{12}C^{15}N^{-}$ signal that localizes ^{15}N-DLPC (A), the $^{13}C^{1}H^{-}$ signal that localizes $^{13}C_{18}$-DSPC (B), and the overlaid $^{12}C^{15}N^{-}$ and $^{13}C^{1}H^{-}$ signals (C). (**D**) An AFM image of the same region on the sample taken before NanoSIMS analysis. The contrast levels within the NanoSIMS images reflect the normalized signal intensity, corresponding to 100 and 0 mol % of the appropriate isotopically labeled lipid, as determined from calibration curves [see text and (*22*)]. Arrows indicate objects in the AFM images that are unlabeled debris, not domains, and their corresponding locations in the NanoSIMS images. Domains with diameters as small as ~100 nm, as measured by AFM, were visible in the SIMS images (e.g., those highlighted with circles). NanoSIMS images were acquired with a pixel size of ~100 nm by 100 nm.

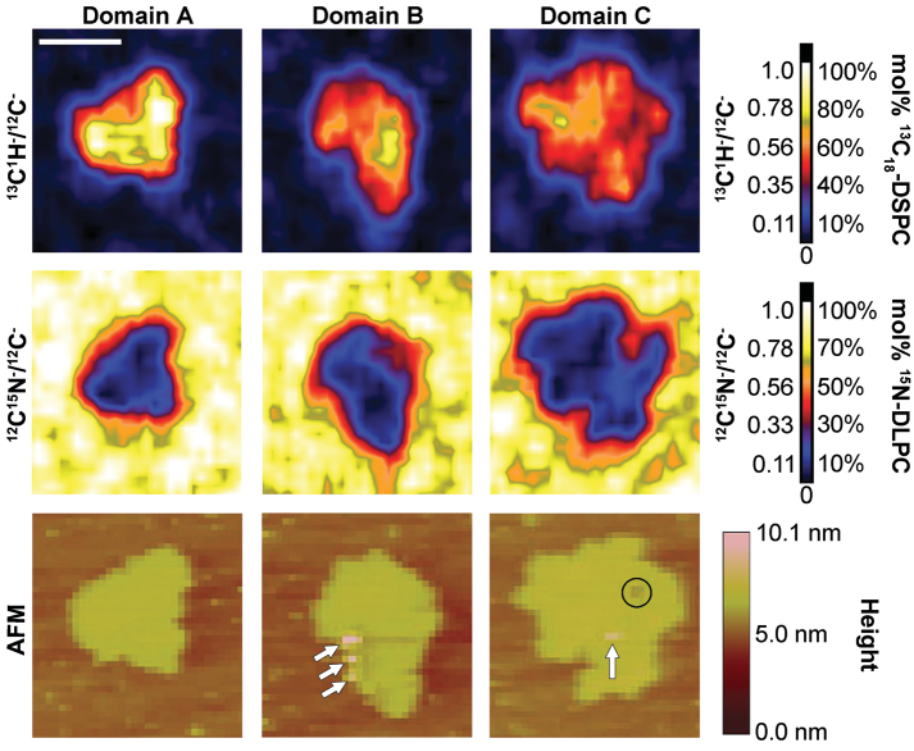

Fig. 3. Details of correlated NanoSIMS and AFM images showing domain composition and topography. The $^{13}C^1H^-/^{12}C^-$ and $^{12}C^{15}N^-/^{12}C^-$ NanoSIMS isotope ratio images show the abundance of $^{13}C_{18}$-DSPC and ^{15}N-DLPC, respectively, within the bilayer, as determined from calibration curves (fig. S3). AFM images acquired at the same sample locations reveal topography. Lower concentrations of both lipids were detected in the locations where debris was identified (arrows). The lipid composition within the gel phase was usually consistent with the phase diagram predictions (domain A), but elevations in the amount of ^{15}N-DLPC within the gel phase were occasionally detected at localized areas within the domains (domains B and C). AFM imaging indicated a small (< 200 nm) depression that could be a fluid-phase subdomain (circle) trapped within the gel phase (domain C); this is confirmed by the NanoSIMS image, which shows an elevated amount of ^{15}N-DLPC across this region (see also Fig. 4). NanoSIMS images were acquired with a pixel size of 100 nm by 100 nm and are smoothed over three pixels. Scale bar, 1 μm.

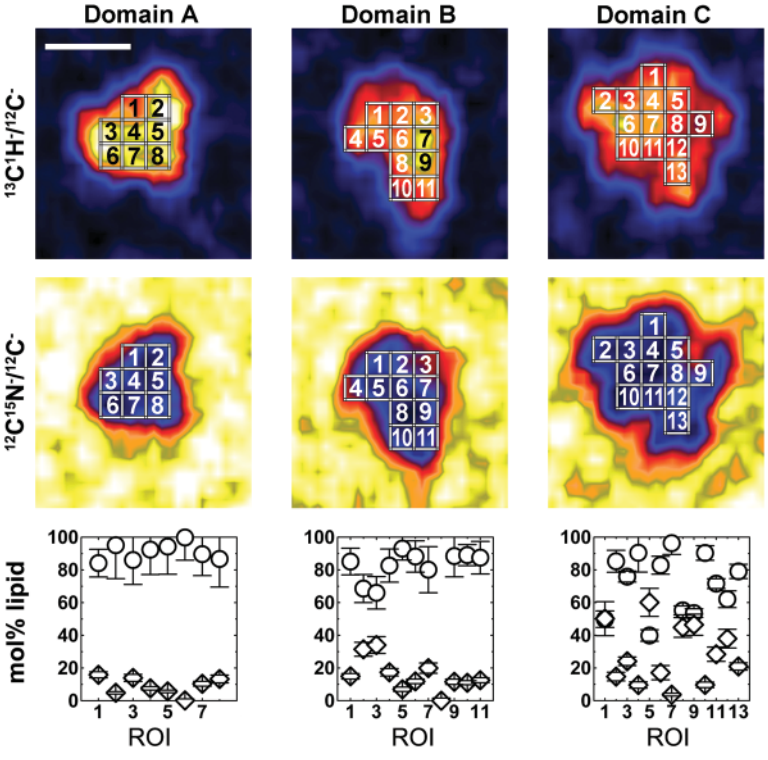

Fig. 4. Quantitative analysis of the gel-phase domains shown in Fig. 3. Each gel-phase domain was divided into regions of 3 pixels by 3 pixels; specific regions of interest (ROIs) within each domain are shown on the NanoSIMS images. The graphs illustrate the amount of $^{13}C_{18}$-DSPC (○) and ^{15}N-DLPC (◇) detected within each domain for the numbered ROI, where each data point represents a region of 3 pixels by 3 pixels within a domain, and the error bars represent the uncertainty calculated from counting statistics (fig. S4) (*22*). Statistically significant lateral variations in lipid composition were detected in domain C, where ROIs 5, 8, and 9 are in the vicinity of the fluid-phase subdomain that was detected by AFM (Fig. 3, domain C, circled region). NanoSIMS images were acquired with a pixel size of 100 nm by 100 nm and are smoothed over three pixels. Scale bar, 1 μm.

ized $^{13}C^1H^-$ or $^{12}C^{15}N^-$ signal intensities ($^{13}C^1H^-/^{12}C^-$ or $^{12}C^{15}N^-/^{12}C^-$) to the mol % of $^{13}C_{18}$-DSPC or ^{15}N-DLPC, respectively, within each sample (fig. S3). With this approach, the gel-phase lipid composition and uniformity were investigated by converting the component-specific secondary ion intensities collected at numerous locations within a single micrometer-sized domain into mol % concentrations (Fig. 3).

We could often detect compositional heterogeneity within the gel phase. Although the majority of the domain consisted of a ~9:1 mol ratio of $^{13}C_{18}$-DSPC to ^{15}N-DLPC, as predicted by the phase diagrams for DSPC and DLPC mixtures (*27*–*29*), higher concentrations of ^{15}N-DLPC were occasionally detected within the gel phase. To determine whether the ^{15}N-DLPC distribution within the gel-phase domains varied in a statistically significant manner, we divided each domain into regions of 3 pixels by 3 pixels that did not include the domain edges or debris (Fig. 4) and used the calibration curves to determine the amount of ^{15}N-DLPC within each region. The variations in the ^{15}N-DLPC content within domains B and C (Fig. 4) were greater than the uncertainty in the measurements, which indicates that these domains contained statistically significant differences in lipid composition. AFM imaging revealed that the elevated ^{15}N-DLPC concentration localized within one $^{13}C_{18}$-DSPC–enriched domain (Figs. 3 and 4, domain C) corresponded to a small (diameter <200 nm) fluid-phase subdomain within the gel phase (Fig. 3, circle). We hypothesize that

small gel-phase domains (tens of nanometers in diameter) that form early in the phase separation process coalesced around a small amount of ^{15}N-DLPC, thereby trapping the fluid-phase subdomain within the growing gel-phase domain [see (*30*) for a theoretical model that may be relevant to this process]. A similar process may have produced the elevated concentrations of ^{15}N-DLPC that were detected at localized regions within other gel-phase domains; however, the absence of topographical features that are characteristic of gel-fluid interfaces at these regions implies that either the fluid-phase subdomains were smaller than the lateral resolution of these AFM images, or the ^{15}N-DLPC was well dispersed within these small regions of the gel phase. [Note that the lateral resolution of these AFM images, ~70 nm, is significantly lower than the highest resolution attainable with AFM because relatively large areas (35 μm by 35 μm) were imaged at 512 pixels by 512 pixels to locate regions for NanoSIMS analysis.] Lower concentrations of both lipids were measured in regions where debris is visible in the AFM images, which indicated that the nonlipid particles were embedded in the bilayer and could have served as nucleation sites. In the fluid phase, the lipid composition was again well approximated by phase diagrams (*27*, *29*); the ratio of ^{15}N-DLPC to $^{13}C_{18}$-DSPC was greater than 19:1, although tiny gel-phase domains scattered throughout the fluid phase may have been included in this value.

With the use of component-specific secondary ion imaging performed with the NanoSIMS, domains as small as ~100 nm in diameter were successfully imaged within a phase-separated lipid membrane, the lipid composition within small regions of the bilayer were quantified, and heterogeneous lipid distributions within gel-phase domains were identified. This example of phase-separated membrane domains also demonstrates the advantage of combining quantitative lipid composition analysis performed by the NanoSIMS with multiple imaging modalities. Because supported lipid bilayers are amenable to isotopic substitution and freeze-drying, this approach can establish the distributions of multiple lipids and membrane-anchored proteins within more complex phase-separated supported membranes by incorporating a distinct stable isotope into each membrane component of interest and simultaneously imaging the secondary ions that distinguish each species. This approach can be extended to living cells by selectively incorporating stable isotopes into membrane components through the use of techniques to label lipid components in live cells (*31*, *32*) as well as by isolating cell membranes with methods to detach intact membrane sheets from live cells (*33*–*36*). In this way, quantitative information on multiple components within native cell membranes may be obtained with high lateral resolution.

References and Notes

1. K. Simons, D. Toomre, *Nat. Rev. Mol. Cell Biol.* **1**, 31 (2000).
2. D. A. Brown, E. London, *Annu. Rev. Cell Dev. Biol.* **14**, 111 (1998).
3. M. Edidin, *Annu. Rev. Biophys. Biomol. Struct.* **32**, 257 (2003).
4. G. W. Feigenson, J. T. Bulboltz, *Biophys. J.* **80**, 2775 (2001).
5. B. Stottrup, D. S. Stevens, S. L. Keller, *Biophys. J.* **88**, 269 (2005).
6. A. K. Kenworthy, N. Petranova, M. Edidin, *Mol. Biol. Cell* **11**, 1645 (2000).
7. J. Korlach, P. Schwille, W. W. Webb, G. W. G. W. Feigenson, *Proc. Natl. Acad. Sci. U.S.A.* **96**, 8461 (1999).
8. N. Kahya, D. Scherfeld, K. Bacia, P. Schwille, *J. Struct. Biol.* **147**, 77 (2004).
9. J. E. Shaw *et al.*, *Biophys. J.* **90**, 2170 (2006).
10. D. C. Fernandez, R. Bhargava, S. M. Hewitt, I. W. Levin, *Nat. Biotechnol.* **23**, 469 (2005).
11. E. O. Potma, X. S. Xie, *ChemPhysChem* **6**, 77 (2005).
12. A. R. Burns, *Langmuir* **19**, 8358 (2003).
13. J. C. Lawrence, D. E. Saslowsky, J. M. Edwardson, R. M. Henderson, *Biophys. J.* **84**, 1827 (2003).
14. C. Yuan, J. Furlong, P. Burgos, L. J. Johnston, *Biophys. J.* **82**, 2526 (2002).
15. N. Bourdos *et al.*, *Biophys. J.* **79**, 357 (2000).
16. A. G. Sostarecz, C. M. McQuaw, A. G. Ewing, N. Winograd, *J. Am. Chem. Soc.* **126**, 13882 (2004).
17. M. L. Pachloski, D. M. Cannon, A. G. Ewing, N. Winograd, *J. Am. Chem. Soc.* **121**, 4716 (1999).
18. J.-L. Guerquin-Kern, T.-D. Wu, C. Quintana, A. Croisy, *Biochim. Biophys. Acta* **1724**, 228 (2005).
19. C. Galli Marxer, M. L. Kraft, P. K. Weber, I. D. Hutcheon, S. G. Boxer, *Biophys. J.* **88**, 2965 (2005).
20. R. Peteranderl, C. Lechene, *J. Am. Soc. Mass Spectrom.* **15**, 478 (2004).
21. S. G. Ostrowski, C. T. Van Bell, N. Winograd, A. G. Ewing, *Science* **305**, 71 (2004).
22. See supporting material on *Science* Online.
23. J. T. Groves, N. Ulman, S. G. Boxer, *Science* **275**, 651 (1997).
24. T. V. Ratto, M. L. Longo, *Biophys. J.* **83**, 3380 (2002).
25. W. C. Lin, C. D. Blanchette, T. V. Ratto, M. L. Longo, *Biophys. J.* **90**, 228 (2006).
26. C. D. Blanchette, W. C. Lin, T. V. Ratto, M. L. Longo, *Biophys. J.* **90**, 4466 (2006).
27. S. Mabrey, J. M. Sturtevant, *Proc. Natl. Acad. Sci. U.S.A.* **73**, 3862 (1976).
28. R. E. Jacobs, B. S. Hudson, H. C. Andersen, *Biochemistry* **16**, 4349 (1977).
29. J. H. Ipsen, O. G. Mouritsen, *Biochim. Biophys. Acta* **944**, 121 (1988).
30. V. A. J. Frolov, Y. A. Chizmadzhev, F. S. Cohen, J. Zimmerberg, *Biophys. J.* **91**, 189 (2006).
31. G. van Echten, R. Birk, G. Brenner-Weiss, R. R. Schmidt, K. Sandhoff, *J. Biol. Chem.* **265**, 9333 (1990).
32. P. Keller, K. Simons, *J. Cell Biol.* **140**, 1357 (1998).
33. S. T. Hess *et al.*, *J. Cell Biol.* **169**, 965 (2005).
34. J. B. Perez, K. L. Martinez, J. M. Segura, H. Vogel, *Adv. Funct. Mater.* **16**, 306 (2006).
35. F. Drees, A. Reilein, W. J. Nelson, *Methods Mol. Biol.* **294**, 303 (2005).
36. S. Yamada, S. Pokutta, F. Drees, W. I. Weis, W. J. Nelson, *Cell* **123**, 889 (2005).

37. We thank W.-C. Lin and C. D. Blanchette for their help in forming phase-separated samples, and L. R. Nittler for the development of the image processing software. Supported by grants from the NSF Biophysics program and NIH grant GM06930 (S.G.B.) and by an NIH National Research Service Award fellowship (M.L.K.). Work at Lawrence Livermore National Laboratory was performed under the auspices of the U.S. Department of Energy under contract W-7405-Eng-4. We thank the Stanford Nanofabrication Facility for fabrication and the NSF Materials Research Science and Engineering Centers, Center on Polymer Interfaces and Macromolecular Assemblies, for analysis (ellipsometry and AFM).

Supporting Online Material

www.sciencemag.org/cgi/content/full/313/5795/1948/DC1
Materials and Methods
Figs. S1 to S4
Tables S1 to S4
References

22 May 2006; accepted 9 August 2006
10.1126/science.1130279

Ultrafast Carbon-Carbon Single-Bond Rotational Isomerization in Room-Temperature Solution

Junrong Zheng, Kyungwon Kwak, Jia Xie, M. D. Fayer

Generally, rotational isomerization about the carbon-carbon single bond in simple ethane derivatives in room-temperature solution under thermal equilibrium conditions has been too fast to measure. We achieved this goal using two-dimensional infrared vibrational echo spectroscopy to observe isomerization between the gauche and trans conformations of an ethane derivative, 1-fluoro-2-isocyanato-ethane (1), in a CCl_4 solution at room temperature. The isomerization time constant is 43 picoseconds (ps, 10^{-12} s). Based on this value and on density functional theory calculations of the barrier heights of 1, *n*-butane, and ethane, the time constants for *n*-butane and ethane internal rotation under the same conditions are ~40 and ~12 ps, respectively.

Many molecules can undergo rotational isomerization around one or more of their chemical bonds. During the course of isomerization, a molecule exchanges between relatively stable conformations by passing through unstable configurations. Rotational isomerization is a major factor in the dynamics, reactivity, and biological activity of a multiplicity of molecular structures. Ethane and its derivatives are textbook examples of molecules that undergo this type of isomerization. (*1*) In ethane, as one of the two methyl groups rotates 360° around the central carbon-carbon single bond, it will alternate three times between an unstable eclipsed conformation and the

Department of Chemistry, Stanford University, Stanford, CA 94305, USA.